A measurement of the scintillation decay time constant of nuclear recoils in liquid xenon with the XMASS-I detector

XMASS Collaboration ; Abe, K. ; Hiraide, K. ; Ichimura, K. ; Kishimoto, Y. ; Kobayashi, K. ; Kobayashi, M. ; Moriyama, S. ; Nakahata, M. ;···

A measurement of the scintillation decay time constant of nuclear recoils in liquid xenon with the XMASS-I detector

To cite this article: K. Abe *et al* 2018 *JINST* **13** P12032

View the article online for updates and enhancements.

Recent citations

- Search for WIMP-129Xe inelastic scattering with particle identification in XMASS-I
  T. Suzuki *et al*

IOP ebooks™

Bringing you innovative digital publishing with leading voices to create your essential collection of books in STEM research.

Start exploring the collection - download the first chapter of every title for free.

A measurement of the scintillation decay time constant of nuclear recoils in liquid xenon with the XMASS-I detector

The XMASS collaboration

K. Abe,[a,d] K. Hiraide,[a,d] K. Ichimura,[a,d] Y. Kishimoto,[a,d] K. Kobayashi,[a,d] M. Kobayashi,[a]
S. Moriyama,[a,d] M. Nakahata,[a,d] H. Ogawa,[a,d,1] K. Sato,[a] H. Sekiya,[a,d] T. Suzuki,[a]
O. Takachio,[a] A. Takeda,[a,d] S. Tasaka,[a] M. Yamashita,[a,d] B.S. Yang,[a,d,2] N.Y. Kim,[b]
Y.D. Kim,[b] Y. Itow,[c,e] K. Kanzawa,[c] K. Masuda,[c] K. Martens,[d] Y. Suzuki,[d] B. D. Xu,[d]
K. Miuchi,[f] N. Oka,[f] Y. Takeuchi,[f,d] Y.H. Kim,[g,b] K.B. Lee,[g] M.K. Lee,[g] Y. Fukuda,[h]
M. Miyasaka,[i] K. Nishijima,[i] K. Fushimi,[j] G. Kanzaki[j] and S. Nakamura[k]

[a]*Kamioka Observatory, Institute for Cosmic Ray Research, the University of Tokyo,*
Higashi-Mozumi, Kamioka, Hida, Gifu, 506-1205, Japan

[b]*Center for Underground Physics, Institute for Basic Science,*
70 Yuseong-daero 1689-gil, Yuseong-gu, Daejeon, 305-811, South Korea

[c]*Institute for Space-Earth Environmental Research, Nagoya University, Nagoya, Aichi 464-8601, Japan*

[d]*Kavli Institute for the Physics and Mathematics of the Universe (WPI), the University of Tokyo,*
Kashiwa, Chiba, 277-8582, Japan

[e]*Kobayashi-Maskawa Institute for the Origin of Particles and the Universe, Nagoya University,*
Furo-cho, Chikusa-ku, Nagoya, Aichi, 464-8602, Japan

[f]*Department of Physics, Kobe University, Kobe, Hyogo 657-8501, Japan*

[g]*Korea Research Institute of Standards and Science, Daejeon 305-340, South Korea*

[h]*Department of Physics, Miyagi University of Education, Sendai, Miyagi 980-0845, Japan*

[i]*Department of Physics, Tokai University, Hiratsuka, Kanagawa 259-1292, Japan*

[j]*Department of Physics, Tokushima University,*
2-1 Minami Josanjimacho Tokushima city, Tokushima, 770-8506, Japan

[k]*Department of Physics, Faculty of Engineering, Yokohama National University,*
Yokohama, Kanagawa 240-8501, Japan

E-mail: xmass.publications12@km.icrr.u-tokyo.ac.jp

---

[1]Now at Department of Physics, College of Science and Technology, Nihon University, Kanda, Chiyoda-ku, Tokyo 101-8308, Japan.

[2]Now at Center for Axion and Precision Physics Research, Institute for Basic Science, Daejeon 34051, South Korea.

https://doi.org/10.1088/1748-0221/13/12/P12032

ABSTRACT: We report an in-situ measurement of the nuclear recoil (NR) scintillation decay time constant in liquid xenon (LXe) using the XMASS-I detector at the Kamioka underground laboratory in Japan. XMASS-I is a large single-phase LXe scintillation detector whose purpose is the direct detection of dark matter via NR which can be induced by collisions between Weakly Interacting Massive Particles (WIMPs) and a xenon nucleus. The inner detector volume contains 832 kg of LXe.

^{252}Cf was used as an external neutron source for irradiating the detector. The scintillation decay time constant of the resulting neutron induced NR was evaluated by comparing the observed photon detection times with Monte Carlo simulations. Fits to the decay time prefer two decay time components, one for each of the Xe_2^* singlet and triplet states, with $\tau_S = 4.3\pm0.6$ ns taken from prior research, τ_T was measured to be $26.9^{+0.7}_{-1.1}$ ns with a singlet state fraction F_S of $0.252^{+0.027}_{-0.019}$. We also evaluated the performance of pulse shape discrimination between NR and electron recoil (ER) with the aim of reducing the electromagnetic background in WIMP searches. For a 50% NR acceptance, the ER acceptance was $13.7\pm1.0\%$ and $4.1\pm0.7\%$ in the energy ranges of 5–$10\,keV_{ee}$ and 10–$15\,keV_{ee}$, respectively.

Contents

1 Introduction

Liquid xenon (LXe) has been used in many modern experiments such as dark matter and neutrino-less double beta decay searches [1–5]. The scintillation timing information can be used for position reconstruction of an event in the detector [6] as well as for particle identification [7]. Studies on the scintillation process in LXe has been conducted in various experiments [8–19]. A scintillation photon is produced by two mechanisms. One is the direct excitation of Xe atoms that then forms an excited dimer Xe_2^*,

$$Xe^* + Xe + Xe \rightarrow Xe_2^* + Xe,$$
$$Xe_2^* \rightarrow 2Xe + h\nu .$$
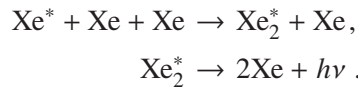
The other process involves the recombination process between electrons and Xe ions

$$Xe^+ + Xe \rightarrow Xe_2^+,$$
$$Xe_2^+ + e^- \rightarrow Xe^{**} + Xe,$$
$$Xe^{**} \rightarrow Xe^* + heat,$$
$$Xe^* + Xe + Xe \rightarrow Xe_2^* + Xe,$$
$$Xe_2^* \rightarrow 2Xe + h\nu .$$
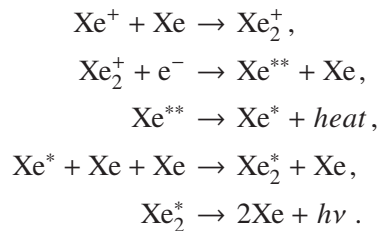
The Xe_2^* dimer has both a singlet and triplet state, each with its own decay time constant. The decay time constants of the singlet and triplet states were reported to be 4.3±0.5 ns and 21±2 ns, respectively using ^{252}Cf fission fragments [10]. While the recombination process has a longer decay time constant of more than 30 ns, measured with 1 MeV electrons from a ^{207}Bi source [10, 11]. In the case of neutron induced NR events, the decay time constant of the triplet state was reported to be ~20 ns both with an applied electric field (0.1–0.5 kV/cm) [13, 14] and without [15, 19]. The decay time constants of the singlet and triplet states depend weakly on the density of the excited species, whereas the ratio of the singlet to triplet state as well as the recombination time depends on the deposited energy density [20]. The time profile of events' scintillation photon hits (pulse shape) may allow for discrimination between NR and ER initiated events [21].

XMASS-I is a large single phase LXe detector, built primarily for dark matter searches, previously reported the Xe_2^* triplet decay time constant of ER events using low energy gamma-rays calibration sources [8]. In this work, we measured the Xe_2^* triplet decay time constant of NR events using an external ^{252}Cf neutron source irradiating the XMASS-I detector and also evaluated the usefulness of pulse shape discrimination (PSD) between NR and ER in the energy region of interest for dark matter searches.

2 Experimental apparatus
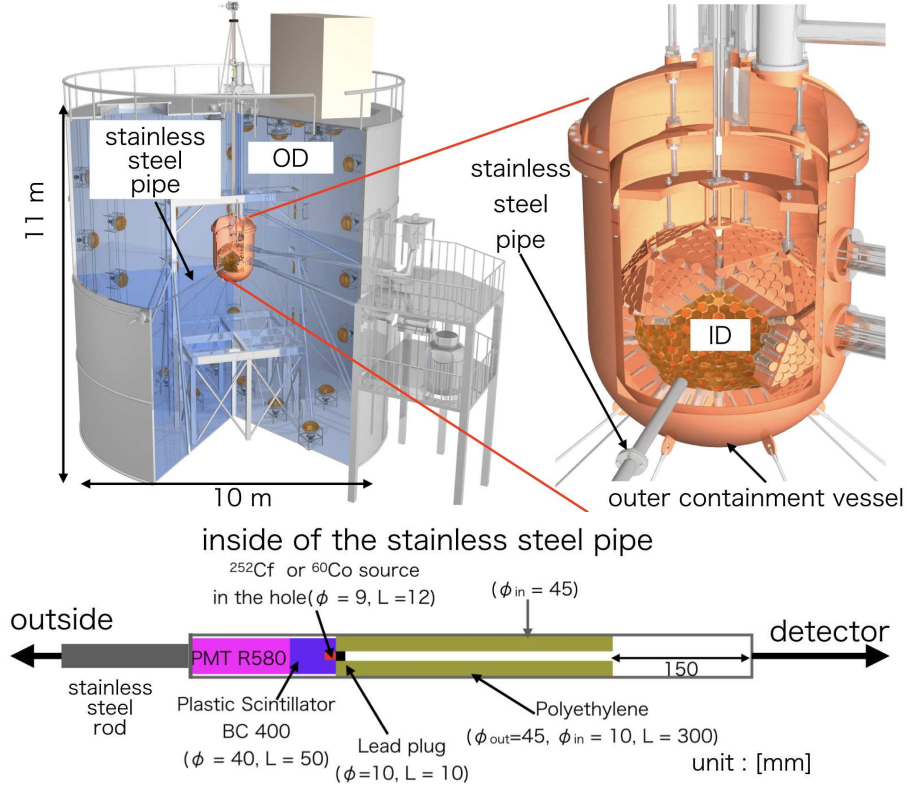
2.1 The XMASS-I detector

The XMASS-I detector is located in the Kamioka mine under 1,000 m of rock (2,700 meter water equivalent). As shown in figure 1, the inner detector (ID) contains 832 kg of LXe inside a spherical, oxygen free high conductivity (OFHC) copper structure with an 80 cm diameter. Scintillation light from the LXe is detected by 630 hexagonal R10789 photomultiplier tubes (PMTs) and 12 cylindrical R10789Mod PMTs with a total photocathode coverage of 62.4%. The inner containment vessel contains the LXe and the PMT holder, while the outer containment vessel holds vacuum for thermal insulation. In order to reduce external gamma-rays and neutrons from the surrounding rock, the ID is placed at the center of the outer detector (OD). The OD is a cylindrical tank 10 m in diameter and 11 m in height filled with ultrapure water. 72 Hamamatsu 20-inch R3600 PMTs are mounted on the inner surface of the water tank to provide an active muon veto. More details can be found in ref. [1].

Signals from the 642 ID PMTs were recorded by CAEN V1751 waveform digitizers with a 1 GHz sampling rate and 10-bit resolution. Analog-timing-modules (ATMs) that were previously used in the Super-Kamiokande experiment [22, 23] worked for generating a trigger. The threshold for an ID PMT to register a hit in the ATMs is set at 0.2 photoelectron (PE). When 4 or more ID PMT hits are observed in a 200 ns coincidence window, a global trigger is issued to both the ATMs and the waveform digitizers. For each triggered event, the waveform is recorded with a width of 10 μs. The OD trigger requires at least 8 PMT hits in a 200 ns coincidence window.

2.2 Detector calibrations

2.2.1 LED calibration

The individual PMT gains are monitored by a blue LED embedded in the inner surface of the PMT holder. This LED is flashed every second using the one-pulse-per-second signal from the global

Figure 1. Schematic view of the XMASS detector and the calibration setup.

positioning system. LED calibration data is taken continually during the physics runs and identified by the trigger information.

2.2.2 Energy calibration and light yield

To check the stability of the detector's light yield, inner calibration data using a ^{57}Co source is taken every one or two weeks. Deploying the ^{57}Co 122 keV gamma-ray source at the center of the detector, we obtain a photoelectron yield of ~15 PE/keV and also trace the timing offsets of the PMT channels. The ^{57}Co source as well as ^{55}Fe, ^{109}Cd, ^{241}Am, and ^{137}Cs are also measured off of center along the detector's z-axis for position dependent energy calibration within the detector.

2.3 The neutron source and its deployment

^{252}Cf undergoes spontaneous fission with a branching ratio of 3.11%. An average fission event emits 8 gamma-rays with a total energy of 7 MeV and 3.75 neutrons [24]. This gamma-ray emission is used to tag such fission events. Figure 1 shows the calibration setup. To detect the gamma-rays, the ^{252}Cf source was deployed in the cylindrical Bicron BC400 plastic scintillator, which is 40 mm in diameter, and 50 mm long. It has a central hole with a diameter of 9 mm and a depth of 12 mm, in which the source is placed. The plastic scintillator was coupled with a Hamamatsu R580 1.5 inch PMT, and hereafter we call it a neutron tagging assembly (NTA). A timing calibration between the plastic scintillator and XMASS-I detector electronics was performed with the ^{60}Co source. The signal of the plastic scintillator was recorded by the same waveform digitizer used for the ID signals.

A cylindrical polyethylene pipe with the outer diameter of 45 mm, the inner diameter of 10 mm, and the length of 300 mm was installed in front of the plastic scintillator and worked as a support structure. A 10 mm long lead plug is used to shield gamma-rays from the source. A stainless steel pipe, with a 45 mm inner diameter passes through the water tank and terminates at 10 mm away from the outer containment vessel. This NTA was inserted into a stainless steel pipe. A stainless steel rod (SUS rod) attached to the NTA can position the NTA 150 mm away from the end of the stainless steel pipe. This distance is set so the detector trigger rate does not exceed 100 Hz; capable rate of the data acquisition (DAQ).

3 Analysis

3.1 Monte Carlo simulations

The XMASS Monte Carlo (MC) simulation is based on Geant4 [25]. It includes a detailed detector geometry, particle tracking, the Xe scintillation process, photon tracking, PMT response, and responses from the electronics. Table 1 summarises the input parameters used in the MC simulation. The optical parameters, such as the absorption and scattering length of LXe, are extracted by the comparison between data and MC simulation of the ^{57}Co calibrations at multiple source positions. Gamma-ray events originating close to the inner detector surface situated between PMTs was used to deduce the copper reflection by comparing the PE spectrum from observed data and MC simulation [6].

Table 1. Summary of input parameters used in the MC simulation. These were obtained by comparing observed data and MC simulations for a range of calibration techniques outlined above.

LXe density	2.89 g/cm^3
Emission spectrum of LXe	Gaussian distribution (ref. [26])
	centered at 174.8 nm, FWHM 10.2 nm
Refractive index of LXe	1.58–1.72 for 183–167 nm
	from direct measurements [27] with a small correction
	considering density dependence
LXe absorption length	852.9 cm
LXe scattering length	52.7 cm
PMT average quantum efficiency	30%
PMT quartz absorption length	14.3 cm at 175 nm, measured by manufacturer
Copper reflectivity	25%

In the MC simulation of the ^{252}Cf calibration, the Brunson model [24] and the Watt spectral model [28] were used for the input energy spectrum of the gamma-rays and the neutrons, respectively. A neutron can either be captured by a xenon nucleus or simply interact with it via elastic or inelastic scattering. The cross sections from both the ENDF/B-VII.0 library, and the G4NDL3.13 library based on the ENDF/B-VI library were used and the results compared in order to evaluate the cross section's systematic uncertainty. We followed the instructions in refs. [29, 30] to use ENDF/B-VII.0 library. In considering NR events, the relative scintillation efficiency L$_{\text{eff}}$ [31], is defined as the

scintillation yield of xenon for NR relative to the zero-field scintillation yield for 122 keV gamma-rays from ^{57}Co. The non-linearity of scintillation yield of ER events over energy was accounted for using a model from ref. [32] tuned with XMASS-I gamma-ray calibration data. Using the measurement setup outlined in figure 1, the rate for multiple neutrons or gamma-rays from the same fission event to enter the ID simultaneously was found to be negligible. Therefore, only an individual neutron or gamma-ray was generated for each MC event in the ^{252}Cf simulation with their intensities considered.

The detection time of the ith photon T^i after a ^{252}Cf spontaneous fission is defined as

$$T^i = t_{\text{Edep}} + t^i_{\text{scinti}} + t^i_{\text{TOF}} + t^i_{\text{TT}} + t^i_{\text{jitter}}. \tag{3.1}$$

t_{Edep} is the time when the incident particle deposits its energy in the LXe. And the LXe scintillation photon emission time t^i_{scinti} follows the scintillation decay time profile parameterized as

$$f(t) = \frac{F_S}{\tau_S} \cdot \exp\left(-\frac{t}{\tau_S}\right) + \frac{1 - F_S}{\tau_T} \cdot \exp\left(-\frac{t}{\tau_T}\right). \tag{3.2}$$

We assumed that the scintillation decay time profile has two decay constants τ_S and τ_T, corresponding to the decay constants of the singlet and the triplet states respectively, and that the fraction of photons generated from decays of singlet dimers F_S and triplet dimers F_T sum to unity ($F_T = 1 - F_S$) following ref. [8]. t^i_{TOF} is the time of flight (TOF) of the scintillation photon. Here, the group velocity of the scintillation light was calculated from the refractive index of LXe. t^i_{TT} is the transit time in the PMT, which we assume to be the same for all PMTs. The transit time spread (TTS) of $\sigma = 2.4$ ns for PMT [33] was included in the timing calculation. t^i_{jitter} is a smearing parameter accounting for the timing jitter in the electronic channel of PMT and extracted from the ^{57}Co calibration data. It follows a Gaussian distribution with a standard deviation of 0.93 ns [8]. After calculating T^i for all photons, a waveform for each PMT was simulated using the one PE pulse (template pulse) shape extracted from LED calibration data. A residual between the template pulse and the real data was found to be $\sigma < 0.1$ PE for all PMTs.

3.2 Event selection

We took 1.5 hours of ^{252}Cf source data with an ID trigger rate of roughly 80 Hz. The signal of the plastic scintillator was searched for by offline analysis. Events related to neutrons from the ^{252}Cf source were selected using the following three criteria. (1) Only the ID trigger is issued to avoid muon or muon induced events. (2) The time difference from the previous ID event is longer than 500 μs and the root mean square of the timings of all hits in the event is less than 100 ns. This cut removes noise events that often follow particularly high energy events. (3) ID trigger is issued between 30 and 100 ns after the NTA trigger (ΔT) to avoid ^{252}Cf gamma-rays induced events. ΔT in MC simulation is calculated from the time difference between particle generation and an ID trigger being issued. Figure 2 shows the ΔT distributions of events which have less than 500 detected PE in the ID. The neutron in a MC event can deposit its energy at a single position or over multiple positions within the LXe. If all of the photons detected originate from a single position they are classed as single-site, if multiple positions then multi-site.

Figure 3 shows the energy spectrum after all cuts. It includes the systematic uncertainties related to the detection efficiency of the plastic scintillator ($\pm 10\%$), the cross section difference
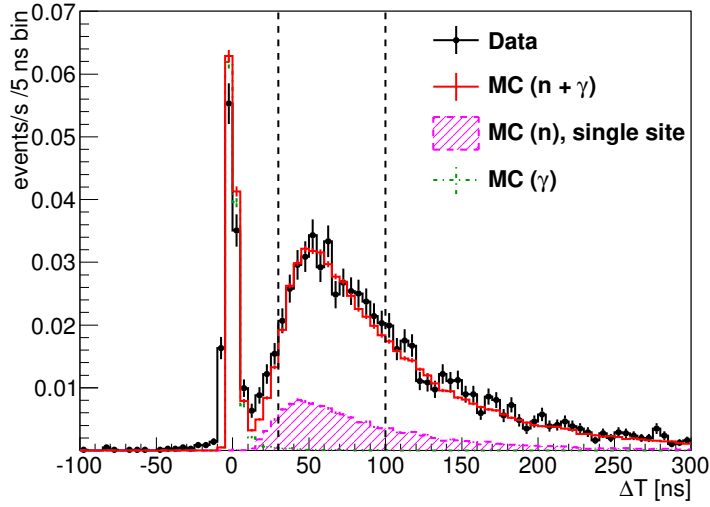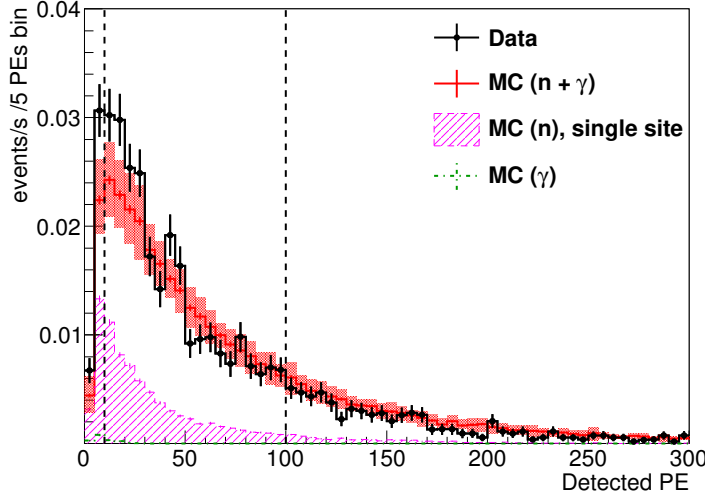
Figure 2. Timing distributions of ^{252}Cf source data (solid black) and MC simulation (solid red). ΔT is defined in section 3.2. The timing of each event is aligned so that the events induced by the ^{252}Cf gamma-rays peak at $\Delta T = 0$ ns. Magenta dotted and green dash-dotted histograms show the timing distribution from the ^{252}Cf neutron simulation (single site events only) and the ^{252}Cf gamma-ray simulation, respectively. The accidental coincidence contribution was derived from the event rate in $-1900 < \Delta T < -100$ ns time window. This accidental rate was about 3×10^{-4} events/s and was subtracted from data. Events in $30 < \Delta T < 100$ ns were used for the NR events analysis.

between the G4NDL3.13 library and the ENDF-B/VII.0 library (25% at most), the scintillation efficiency for NR ($\pm 1\sigma$ in ref. [31], 10% at most). We observed a discrepancy (5% at most) in the mean observed PE between the ^{57}Co calibration data and MC simulation at large radii (> 40 cm). This was included as a systematic uncertainty in the MC simulation in figure 3. The detection efficiency and tagging threshold of the plastic scintillator were estimated to be (70±10)% and 100 keV in gamma-ray energy, respectively, by comparing the data from ^{137}Cs and ^{60}Co to MC simulations using a small setup. The ΔT distribution of the MC simulation agreed with data as shown in figure 2. There was about 25% count rate difference below 20 detected PEs in the energy spectra in figure 3, we discuss its impact on the decay time constant in section 4.1.

Multi-site events make up about 75% of the neutron events as deduced from MC simulation. Events with PE counts between 10 and 100 PEs, corresponding to the energy range from 1.5 keV$_{ee}$ (6.3 keV$_{nr}$) to 8.3 keV$_{ee}$ (40 keV$_{nr}$), were used to evaluate the NR decay constant described in the following section.

3.3 Evaluation of the nuclear recoil decay time constant

The scintillation decay time constant of NR was evaluated by comparing the time-distributions of the detected PE over all PMTs and events between data and MC simulation with various timing parameters. To analyze waveforms of individual PMTs, we developed a peak finding algorithm based on a Savitzky-Golay filter [34] to obtain individual photon hit timings. Each peak was fitted with a single PE waveform template obtained from the LED calibration data. Figure 4 shows a

Figure 3. Detected PE distributions of ^{252}Cf source data (solid black) and MC simulation (solid red). The red band shows the quadratic sum of the systematic uncertainty and the statistical uncertainty of the MC simulation. The magenta hashed histogram and the green dash-dotted histogram show the single-site events from the ^{252}Cf neutron simulation, ^{252}Cf gamma-rays simulation, respectively. The contribution of the accidental coincidence events was derived from events in $-1900 < \Delta T < -100$ ns time window and was subtracted from data. Events with PE counts between 10 and 100 PEs were used for NR events analysis.

NR event waveform from a single PMT with the fitting result. Due to fluctuations of the baseline and electronic noise, the peak-finding algorithm sometimes misidentifies the tail of the single PE distribution as a peak. Such misidentified peaks typically have PE smaller than 0.5 PE. In this study, only peaks that have more than 0.5 PE are used. For each event, all peaks from all PMTs are sorted in order of detected timings. The timing of the fourth earliest peak is set to $T = 0$ ns with all other peak timings within the event shifted relative to this time, reflecting the trigger implementation in DAQ. This allows to superimpose all the recorded peak times over events.

To obtain the scintillation decay time constant for NR, we performed a χ^2 fit defined as

$$\chi^2 = \sum_i \frac{(N_i^{\text{data}} - N_i^{\text{MC}} \cdot S)^2}{\sigma_{\text{stat(data)}}^2 + \sigma_{\text{stat(MC)}}^2 \cdot S^2}, \tag{3.3}$$

where N_i^{data} and N_i^{MC} are the number of detected peaks in the ith time bin over all of the data and simulated MC, respectively. S is a free variable for normalization. $\sigma_{\text{stat(Data)}}$ and $\sigma_{\text{stat(MC)}}$ represent the statistical uncertainty in the data sample and the MC simulation, respectively.

The time bin width was 1 ns and the χ^2 is calculated in the range of $3 \leq T \leq 120$ ns. To evaluate the scintillation decay time constant for NR, we scanned the parameter F_S from 0.0 to 0.5 in steps of 0.025, and τ_T from 21.0 to 30.5 ns in steps of 0.5 ns in MC simulation. For τ_S, we used 3.7, 4.3, and 4.9 ns taken from ref. [10].
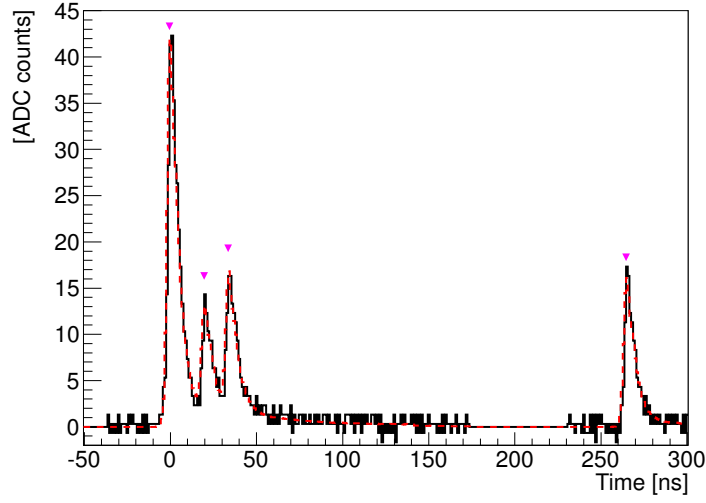
Figure 4. A raw waveform in a single PMT in a ^{252}Cf calibration event. To reduce data size, parts of a waveform that do not exceed a threshold of 3 ADC counts were not recorded. The magenta triangles show the detected peaks. The dashed red line shows the waveform reconstruction obtained as the sum of each peak's single-PE waveform fit. A typical single-PE pulse has a height of about 22.4 ADC counts after digitization.
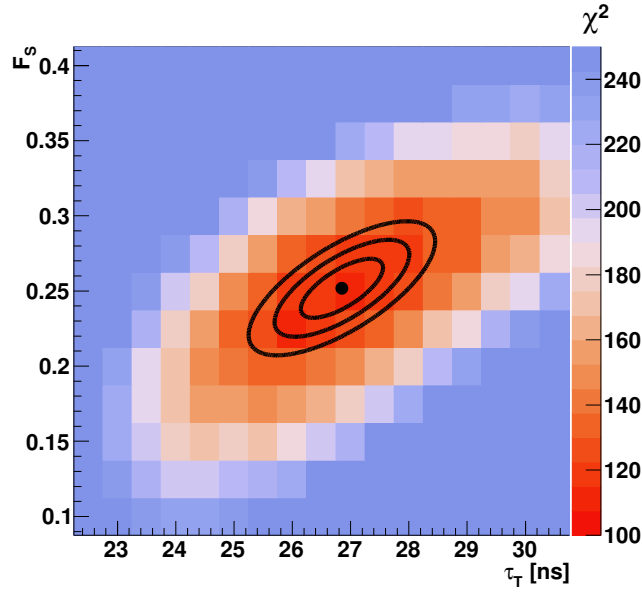
Figure 5. χ^2 map in the F_S and τ_T plane with $\tau_S = 4.3$ ns. Black contours correspond to 1σ, 2σ, and 3σ and are derived from a parabolic function fit described in eq. (4.1). The black point of (26.9 ns, 0.252) for (τ_T, F_S) is the best fit value from the parabolic function fit.
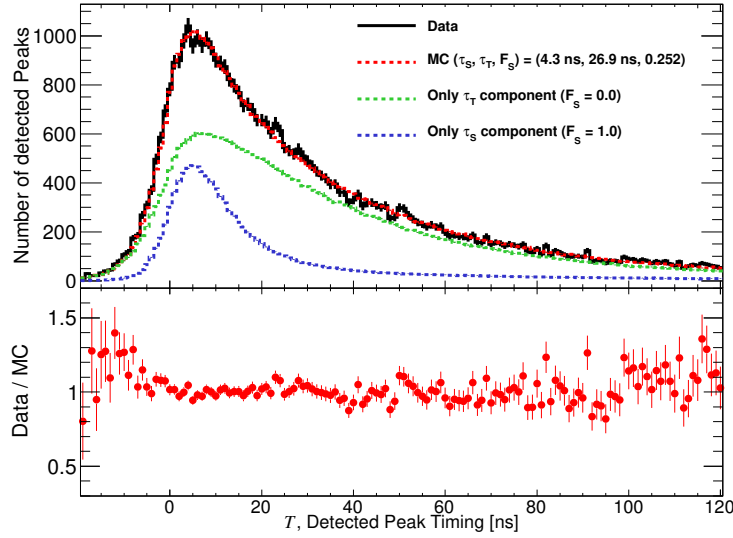
Figure 6. (Top) Pulse timing distributions of data (black) and the best fit MC simulation (red) $(\tau_S, \tau_T, F_S) = (4.3\,\text{ns}, 26.9\,\text{ns}, 0.252)$. This MC distribution's two components are also shown separately in green (τ_T) and blue (τ_S). (Bottom) The ratio of data to the best fit MC simulation.

4 Result and discussion

4.1 The scintillation decay time constant of the nuclear recoil

Figure 5 shows the χ^2 map in the F_S–τ_T plane. Since the parameters were scanned in discrete steps, a parabolic function fit as defined in eq. (4.1) was performed to obtain the scintillation decay time constant.

$$
\begin{aligned}
\chi^2 &= a \cdot (\tau_T')^2 + b \cdot (F_S')^2 + \chi^2_{\min}, \quad \text{where} \\
\tau_T' &= (\tau_T - \tau_T^{\text{best}}) \cdot \cos\theta + (F_S - F_S^{\text{best}}) \cdot \sin\theta \quad \text{and} \\
F_S' &= -(\tau_T - \tau_T^{\text{best}}) \cdot \sin\theta + (F_S - F_S^{\text{best}}) \cdot \cos\theta \ .
\end{aligned}
\tag{4.1}
$$

Here a, b, $\chi^2_{\min}$, θ, τ_T^{best} and F_S^{best} are free parameters in the fit. The section of the parameter plane that has $\chi^2 - \chi^2_{\min} < 20$ in figure 5 was used for this fit. From this parabolic fit, (τ_S, τ_T, F_S) were discovered to be (4.3 ns, 26.9±0.5 ns (stat), 0.252±0.013 (stat)) with the minimum χ^2/ndf = 113.9/115. Data overlaid with the best fit MC simulation is shown in figure 6.

All systematic uncertainties are listed in table 2. They were evaluated as follows:

(1) τ_S: $\tau_S = 4.3 \pm 0.6$ ns from ref. [10] was used in this analysis. The systematic uncertainty introduced by τ_S was evaluated by changing τ_S from 4.3 ns to 3.7 ns and 4.9 ns.

(2) *Neutron cross section*: the event rate, including the fraction of multi-site events, depends on the neutron cross-section. We found an event rate difference of about 10% between the MC simulation using the ENDF-B/VII.0 and the MC simulation using the G4NDL3.13 library. Parameter scans of F_S and τ_T with the G4NDL3.13 library were conducted, and the difference of the respective best fit value was used as the systematic uncertainty due to the neutron cross section. The effect of the count rate difference mentioned in section 3.2 was also evaluated.

**Table 2**. Summary of systematic uncertainties on τ_T and F_S.

Error source	σ_{τ_T} (ns)	σ_{F_S}
τ_S	+0.5, -0.2	+0.009, -0.003
Neutron cross section	+0.2, -0.0	+0.006, -0.000
L_{eff}	+0.0, -0.7	+0.019, -0.010
Jitter	+0.1, -0.2	+0.009, -0.010
After/Pre-pulse	+0.0, -0.6	+0.000, -0.001
Total	+0.5, -1.0	+0.024, -0.014

We evaluated the impact on the scintillation decay time constant by lowering the weight of events in the data below 20 PEs and it turned out to be a negligible effect.

(3) L_{eff}: following ref. [31]'s error estimates, we ran MC simulations also with L_{eff} ±1 σ. We used the difference of the respective best fit values as the systematic uncertainty due to L_{eff}.

(4) *Jitter*: timing jitter affects the determination of the rising edge of timing distributions. The uncertainty was evaluated by comparing the timing distribution of data and simulated samples with different assumptions for the amount of timing jitter. t_{jitter} was changed from $\sigma = 0.93$ ns to 0.0, 0.5, 1.5 ns and the differences of the respective best fit value were assigned as systematic uncertainty.

(5) *After-pulse and pre-pulse*: occasionally single-PE pulses are observed prior to or after the main event pulse, these are aptly labeled pre-pulses and after-pulses, respectively. Their rate and timing information was measured independently in a laboratory setup. The pre-pulses were found to have a 0.10% /PE probability of occurring and on average are located ~15 ns before the main pulse in a time width of ~2 ns. After-pulses have a probability of 0.65% /PE and are located ~40 ns after in a time width of ~5 ns. To study their impact, we generated single-PE pulse timings at the appropriate rate using a Gaussian distribution centered at 40 ns with a 5 ns width and another at -15 ns with a 2 ns width for the after-pulses and pre-pulses, respectively. The differences of the best fit values between using the standard MC PE pulse times and these same times augmented with generated pre-pulse and after-pulse times is used for their systematic uncertainty.

After adding these systematic uncertainties in quadrature, the scintillation decay time constant for NR was estimated to be $(\tau_T, F_S) = (26.9 \pm 0.5 \text{ (stat)}^{+0.5}_{-1.0} \text{ (sys) ns}, 0.252 \pm 0.013 \text{ (stat)}^{+0.024}_{-0.014} \text{ (sys)})$ with $\tau_S = 4.3 \pm 0.6$ ns.

The obtained τ_T is close to that for ER ($27.8^{+1.5}_{-1.1}$ ns using ^{55}Fe 5.9 keV gamma-rays) reported in ref. [8], although the obtained F_S is larger than that of ER ($0.145^{+0.022}_{-0.020}$ using ^{55}Fe 5.9 keV gamma-ray). Figure 7 shows τ_T and F_S for various NR and ER measurements. This measurement had the lowest energy threshold of all the experiments conducted without an external electric field. D. Akimov et al. reported a scintillation decay time constants using a single component exponential fit [15]. The single component fit value of $\tau = 22.5$ ns for $1.5 < E < 8.3$ keV$_{ee}$ in this work is close to their reported value, although the MC simulation does not reproduce the data
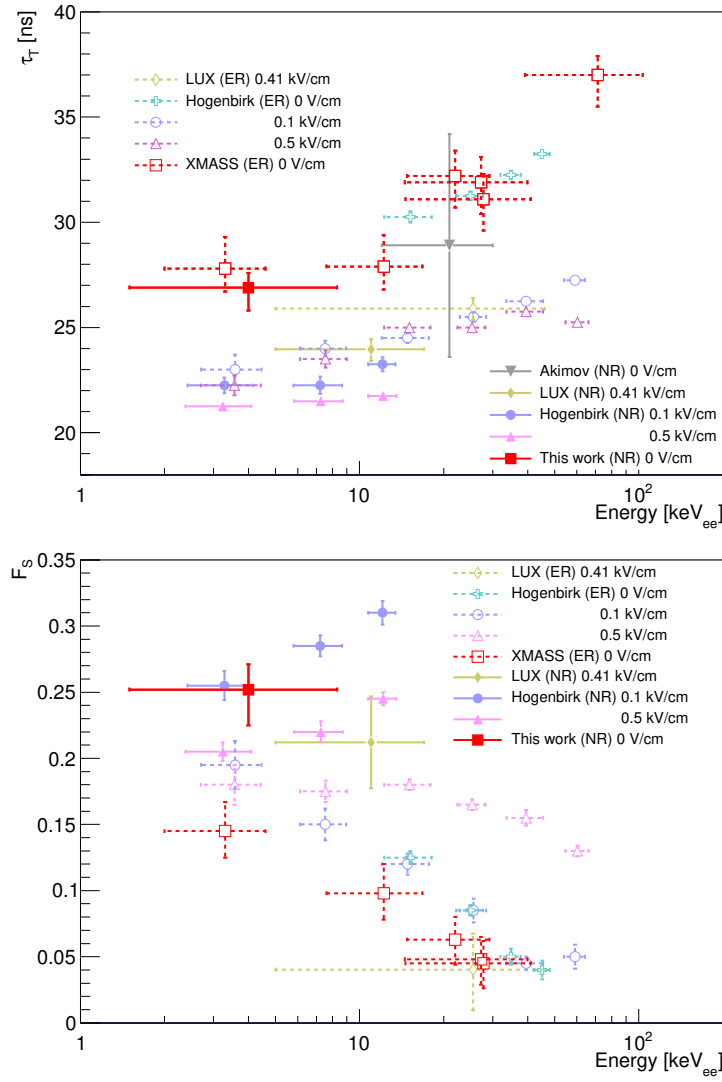
Figure 7. The best-fit parameters τ_T and F_S for various measurements. Filled markers and solid lines correspond to NR measurements. Open markers and dotted lines correspond to ER measurements. Results from Akimov et al. [15], Teymourian et al. [17], the LUX experiment [13], Hogenbirk et al. (0 V/cm, 0.1 kV/cm and 0.5 kV/cm) [14], and XMASS measurement (This work and [8]) are indicated by the black triangle, cyan cross, yellow diamond, green cross, blue circle, magenta triangle, and red square, respectively.

well (χ^2/ndf = 368.1/116). The singlet fraction obtained in this work agrees with the results of refs. [13, 14], however, the τ_T is about 5 ns longer than those values. The τ_T discrepancy might stem from a time delay introduced by the recombination process, which is suppressed under an electric field. The recombination process contributes at most 10% of total scintillation light for nuclear recoil [35]. For alpha particles and ^{252}Cf fission fragments, this process is thought to be very fast and also have only a minor influence, for these species τ_T was reported as 22±1.5 ns and 21±2 ns, respectively [10] without an applied electric field.
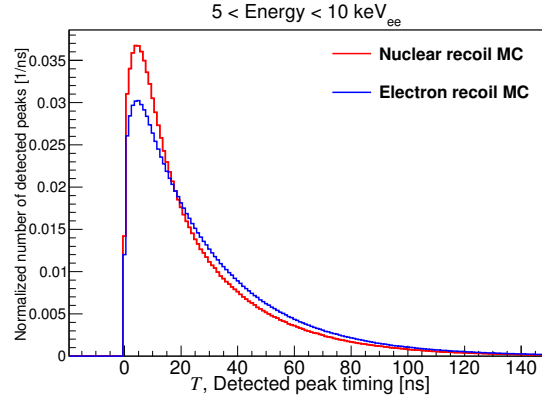
Figure 8. Pulse timing distribution of the simulated ER and NR events with energy deposition from 5 to 10 keV$_{ee}$. In this figure, TOF was subtracted and the timing of the fourth earliest peak in each event was shifted to T=0 ns to reflect the trigger implementation. Areas are normalized to 1.

## 4.2 Performance of the pulse shape discrimination

For Weakly Interacting Massive Particle (WIMP) searches in data from a single phase LXe detector, the possibility of PSD between NR and ER is of significant interest. We evaluated the performance of PSD in XMASS-I based on our scintillation decay time constant measurement. To obtain the relevant timing distributions, we first simulated the ER events with uniform energy from 0 to 20 keV and NR events which followed the energy distribution of 100 GeV/c^2 WIMPs elastically scattering in the LXe target at the center of the detector. Figure 8 shows the peak timing distributions of those simulated ER and NR events that had energy deposits from 5 to 10 keV$_{ee}$. In Figure 8, TOF was subtracted using the velocity of 110 mm/ns for light in LXe and the timing of the fourth earliest peak in each event was set to $T = 0$ ns again to reflect the trigger implementation in DAQ. As mentioned in section 4.1, F$_S$ in NR is larger than in ER. Therefore a difference in the timing distributions can clearly be seen. These histograms in figure 8 were used as the probability density function ($f_{ER,NR}(t_i)$) of the PMTs hit timings and we evaluated the following log likelihood ratio

$$\ln\left(\frac{L_{NR}}{L_{ER}}\right) = \sum \ln(f_{NR}(t_i)) - \sum \ln(f_{ER}(t_i)) \, . \tag{4.2}$$

This log likelihood ratio was calculated using PMT hit times $T > 0$ ns, after TOF subtraction and T$_0$ determination. TOF subtraction uses the reconstructed event position. The performance of this PSD method was evaluated using another MC simulation. Electron events and NR events where simulated with the same energy distributions as before, but now generated uniformly throughout the detector. Figure 9 shows the log likelihood ratio distribution of the simulated ER and NR events that have energy deposits from 5 to 10 keV$_{ee}$ and were reconstructed within 20 cm from the detector center, these events were used for the evaluation of the PSD performance.

The ER acceptances when requiring a 50% NR acceptance for energies between 5 to 10 keV$_{ee}$ and between 10 to 15 keV$_{ee}$ were estimated to be 13.7±1.0% and 4.1±0.7%, respectively. This corresponds to a S/$\sqrt{N}$ ratio of 1.4 and 2.5, respectively. In figure 10 the blue curve shows the ER acceptance as a function of energy. The performance of this PSD method when evaluated using the XMASS-I detector simulation is consistent with the performance that we reported previously
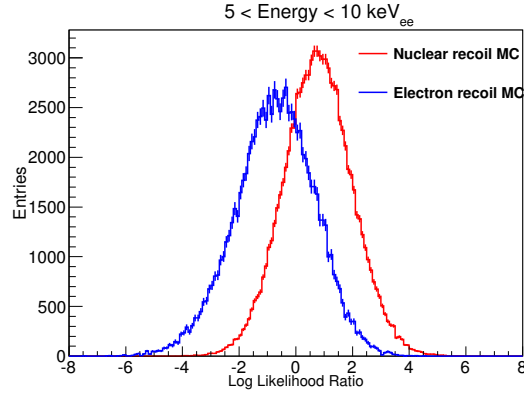
Figure 9. Log likelihood ratio distributions of simulated ER (blue) and NR events (red) reconstructed within a 20 cm radius from the detector center. A positive (negative) log likelihood ratio corresponds to NR (ER) like events.
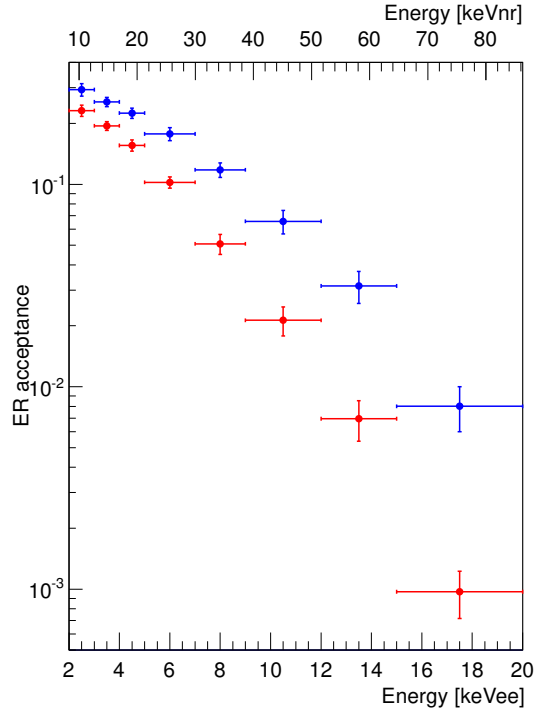
Figure 10. ER acceptance as a function of energy. NR equivalent energy is indicated on the top scale. WIMPs with a mass of $100 \, \text{GeV/c}^2$ were used in the NR simulation. Electrons with energy distributed uniformly between 0 and 20 keV were used in the ER simulation. Both MC simulations generated uniformly distributed events within the XMASS-I detector and events which were reconstructed within 20 cm from the detector center were used for the evaluation. The two curves correspond to the log likelihood performance evaluated for a 50% NR acceptance. Error bars show the quadratic sum of systematic uncertainty and statistical uncertainty. The blue curve shows the result of XMASS-I detector, and the red one represents an ideal case where measurements are not affected by timing jitter in the electronics and TTS in the PMTs.

using a small chamber [21]. We also evaluated the performance of this PSD in an ideal case where the measurement is not affected by the timing jitter or TTS (red curve in figure 10). In this ideal case, the PSD performance improves by about a factor of 2 between 5 and $7\,\mathrm{keV_{ee}}$, and by about one order of magnitude between 15 and $20\,\mathrm{keV_{ee}}$.

5 Conclusions

We evaluated the time profile of NR scintillation emission in LXe with the XMASS-I detector using ^{252}Cf sources. Two decay components are needed to reproduce the timing distribution of the NR data. We obtained the decay time constant of triplet state $\tau_T = 26.9 \pm 0.5$ (stat)$^{+0.5}_{-1.0}$ (sys) ns and the singlet fraction $F_S = 0.252 \pm 0.013$ (stat)$^{+0.024}_{-0.014}$ (sys) with a decay time constant of singlet state $\tau_S = 4.3 \pm 0.6$ ns taken from a prior research. This measurement had the lowest energy threshold without an aplied electric field. We also developed a PSD method based on a log likelihood ratio. The ER acceptances with a 50% NR acceptance at energies between 5 and $10\,\mathrm{keV_{ee}}$ and between 10 and $15\,\mathrm{keV_{ee}}$ were estimated to be $13.7 \pm 1.0\%$ and $4.1 \pm 0.7\%$, respectively.

References

[1] K. Abe et al., *XMASS detector*, *Nucl. Instrum. Meth.* **A 716** (2013) 78 [arXiv:1301.2815].

[2] LUX collaboration, D.S. Akerib et al., *The Large Underground Xenon (LUX) Experiment*, *Nucl. Instrum. Meth.* **A 704** (2013) 111 [arXiv:1211.3788].

[3] PandaX collaboration, X. Cao et al., *PandaX: A Liquid Xenon Dark Matter Experiment at CJPL*, *Sci. China Phys. Mech. Astron.* **57** (2014) 1476 [arXiv:1405.2882].

[4] XENON collaboration, E. Aprile et al., *The XENON1T Dark Matter Experiment*, *Eur. Phys. J.* **C 77** (2017) 881 [arXiv:1708.07051].

[5] M. Auger et al., *The EXO-200 detector, part I: Detector design and construction*, 2012 *JINST* **7** P05010 [arXiv:1202.2192].

[6] XMASS collaboration, K. Abe et al., *A direct dark matter search in XMASS-I*, arXiv:1804.02180.

[7] XMASS collaboration, K. Abe et al., *Improved search for two-neutrino double electron capture on* ^{124}*Xe and* ^{126}*Xe using particle identification in XMASS-I*, *PTEP* **2018** (2018) 053D03 [arXiv:1801.03251].

[8] XMASS collaboration, H. Takiya et al., *A measurement of the time profile of scintillation induced by low energy gamma-rays in liquid xenon with the XMASS-I detector*, *Nucl. Instrum. Meth.* **A 834** (2016) 192 [arXiv:1604.01503].

[9] S. Kubota, M. Hishida and J. Raun, *Evidence for a triplet state of the self-trapped exciton states in liquid argon, krypton and xenon*, *J. Phys.* **C 11** (1978) 2645.

[10] A. Hitachi, T. Takahashi, N. Funayama, K. Masuda, J. Kikuchi and T. Doke, *Effect of ionization density on the time dependence of luminescence from liquid argon and xenon*, *Phys. Rev.* **B 27** (1983) 5279.

[11] S. Kubota, M. Hishida, M. Suzuki and J.-z. Ruan(Gen, *Dynamical behavior of free electrons in the recombination process in liquid argon, krypton and xenon*, *Phys. Rev.* **B 20** (1979) 3486.

[12] J.W. Keto et al., *Exciton lifetimes in electron beam excited condensed phases of argon and xenon*, *J. Chem. Phys.* **71** (1979) 2676.

[13] LUX collaboration, D.S. Akerib et al., *Liquid xenon scintillation measurements and pulse shape discrimination in the LUX dark matter detector*, *Phys. Rev.* **D 97** (2018) 112002 [arXiv:1802.06162].

[14] E. Hogenbirk, J. Aalbers, P.A. Breur, M.P. Decowski, K. van Teutem and A.P. Colijn, *Precision measurements of the scintillation pulse shape for low-energy recoils in liquid xenon*, 2018 *JINST* **13** P05016 [arXiv:1803.07935].

[15] D. Akimov et al., *Measurements of scintillation efficiency and pulse shape for low-energy recoils in liquid xenon*, *Phys. Lett.* **B 524** (2002) 245 [hep-ex/0106042].

[16] J.V. Dawson et al., *A study of the scintillation induced by alpha particles and gamma rays in liquid xenon in an electric field*, *Nucl. Instrum. Meth.* **A 545** (2005) 690 [physics/0502026].

[17] A. Teymourian et al., *Characterization of the QUartz Photon Intensifying Detector (QUPID) for Noble Liquid Detectors*, *Nucl. Instrum. Meth.* **A 654** (2011) 184 [arXiv:1103.3689].

[18] I. Murayama and S. Nakamura, *Time profile of the scintillation from liquid and gaseous xenon*, *Nucl. Instrum. Meth.* **A 763** (2014) 533.

[19] K. Ueshima, *Study of pulse shape discrimination and low background techniques for liquid xenon dark matter detectors*, Ph.D. Thesis, The University of Tokyo, Tokyo Japan (2010), http://www-sk.icrr.u-tokyo.ac.jp/xmass/_pdf/publist/ueshima_PhD.pdf.

[20] E. Aprile and T. Doke, *Liquid Xenon Detectors for Particle Physics and Astrophysics*, *Rev. Mod. Phys.* **82** (2010) 2053 [arXiv:0910.4956].

[21] XMASS collaboration, K. Ueshima et al., *Scintillation-only Based Pulse Shape Discrimination for Nuclear and Electron Recoils in Liquid Xenon*, *Nucl. Instrum. Meth.* **A 659** (2011) 161 [arXiv:1106.2209].

[22] H. Ikeda, M. Mori, T. Tanimori, K.-i. Kihara, Y. Suzuki and Y. Haren, *Front end hybrid circuit for Super-Kamiokande*, *Nucl. Instrum. Meth.* **A 320** (1992) 310.

[23] SUPER-KAMIOKANDE collaboration, Y. Fukuda et al., *The Super-Kamiokande detector*, *Nucl. Instrum. Meth.* **A 501** (2003) 418.

[24] T.E. Valentine, *Evaluation of prompt fission gamma rays for use in simulating nuclear safeguard measurements*, *Ann. Nucl. Eng.* **28** (2001) 191.

[25] GEANT4 collaboration, S. Agostinelli et al., *GEANT4: A Simulation toolkit*, *Nucl. Instrum. Meth.* **A 506** (2003) 250.

[26] K. Fujii et al., *High-accuracy measurement of the emission spectrum of liquid xenon in the vacuum ultraviolet region*, *Nucl. Instrum. Meth.* **A 795** (2015) 293.

[27] S. Nakamura et al., *Measurements of optical properties of liquid xenon scintillator*, in *Proceedings of Workshop on Ionization and Scintillation Counters and Their Uses*, Waseda University Tokyo Japan (2007), pg. 27.

[28] F.H. Fröhner, *Evaluation of ^{252}Cf Prompt Fission Neutron Data from 0 to 20 MeV by Watt Spectrum Fit*, *Nucl. Sci. Eng.* **106** (1990) 345.

[29] E. Mendoza, D. Cano-Ott, C. Guerrero and R. Capote, *New Evaluated Neutron Cross Section Libraries for the GEANT4 Code*, IAEA technical report INDC(NDS)-0612 (2012).

[30] E. Mendoza, D. Cano-Ott, T. Koi and C. Guerrero, *New Standard Evaluated Neutron Cross Section Libraries for the GEANT4 Code and First Verification*, *IEEE Trans. Nucl. Sci.* **61** (2014) 2357.

[31] XENON100 collaboration, E. Aprile et al., *Dark Matter Results from 100 Live Days of XENON100 Data*, *Phys. Rev. Lett.* **107** (2011) 131302 [arXiv:1104.2549].

[32] T. Doke et al., *Non-proportionality of the scintillation yield in liquid xenon and its effect on the energy resolution for gamma-rays*, in *Proceedings of the International Workshop on Technique and Application of Xenon Detectors (Xenon 01)*, Kashiwa Japan (2001), World Scientific, River Edge U.S.A. (2003), pg. 17.

[33] XMASS collaboration, H. Uchida et al., *Search for inelastic WIMP nucleus scattering on ^{129}Xe in data from the XMASS-I experiment*, *PTEP* **2014** (2014) 063C01 [arXiv:1401.4737].

[34] A. Savitzky and M.J.E. Golay, *Smoothing and Differentiation of Data by Simplified Least Squares Procedures*, *Anal. Chem.* **6** (1964) 1627.

[35] E. Aprile et al., *Simultaneous measurement of ionization and scintillation from nuclear recoils in liquid xenon as target for a dark matter experiment*, *Phys. Rev. Lett.* **97** (2006) 081302 [astro-ph/0601552].